A Novel Region Reconstruction Method for Fluorescence Molecular Tomography

Yu An, Jie Liu*, Guanglei Zhang, Jinzuo Ye, Yang Du, Yamin Mao, Chongwei Chi*, and Jie Tian*, *Fellow, IEEE*

***Abstract*—Fluorescence molecular tomography (FMT) could exploit the distribution of fluorescent biomarkers that target tumors accurately and effectively, which enables noninvasive real-time 3-D visualization as well as quantitative analysis of small tumors in small animal studies *in vivo*. Due to the difficulties of reconstruction, continuous efforts are being made to find more practical and efficient approaches to accurately obtain the characteristics of fluorescent regions inside biological tissues. In this paper, we propose a region reconstruction method for FMT, which is defined as an L1-norm regularization piecewise constant level set approach. The proposed approach adopts *a priori* information including the sparsity of the fluorescent sources and the fluorescent contrast between the target and background. When the contrast of different fluorescent sources is low to a certain degree, our approach can simultaneously solve the detection and characterization problems for the reconstruction of FMT. To evaluate the performance of the region reconstruction method, numerical phantom experiments and *in vivo* bead-implanted mouse experiments were performed. The results suggested that the proposed region reconstruction method was able to reconstruct the features of the fluorescent regions accurately and effectively, and the proposed method was able to be feasibly adopted in *in vivo* application.**

***Index Terms*—Fluorescence molecular tomography, piecewise constant level set, 3-D reconstruction.**

I. Introduction

With the high sensitivity and low cost, especially with the rapid development of fluorescent probes and reporter techniques [1]–[3], fluorescence molecular imaging (FMI) has played an increasingly important role in revealing the dynamic interactions of cellular processes [4]–[9]. FMI utilizes an ultrasensitive charge-coupled device (CCD) camera and high performance lasers to detect light emitted from living cells with fluorescence expression. Based on FMI, fluorescence molecular tomography (FMT) is an imaging modality aimed at achieving 3-D visualization of fluorescence regions in tissues *in vivo* through the solution of the reconstruction problem [10]–[12]. Because of its high sensitivity and low cost, the novel optical molecular modality and its applications have been widely used in small animal research and preclinical diagnostics. However, there are still some challenging problems in FMT as following.

One of the problems in FMT is highly ill-posed and ill-conditioned inverse problem, due to that multiple scatterings of photons propagate through heterogeneous biological tissues [13]–[15], and uncertainty of light propagation inside the deep tissue. Even though more fluorescence information can be captured by multiple spatial patterns of illumination, the problem may still be strongly ill-posed because of the sensitivity to noise and errors caused in the data-gathering process and raw data discretization [16]. Appropriate priors or penalties are needed to facilitate reconstruction and to restrict the search space to a specific solution set. According to the existing literatures, multitypes of *a priori* information have been adopted in reconstruction algorithms of FMT ranging from multispectral information to more involved sparse constraint [17]–[22]. The basic idea is to reduce the number of unknown variables or to increase the amount of measurements. Recently, the level set strategy has gained its popularity in image reconstruction. Classical level set methods were developed for modeling propagation of curves by Osher and Sethian [23] and have been widely used in image processing applications [24], [25] and a variety of inverse problems [26]–[28]. They provide a topologically flexible shape-based formulation, elegantly representing multiple objects with complicated geometries. Being different from the standard level set methods, the piecewise constant level set (PCLS) has been discussed in the field of image reconstruction [29]–[32]. It requires only one level set function to identify an arbitrary number of phases, which makes it simpler and require less storage capacity.

The other difficulty is that the numerical computation of reconstruction can be time-consuming and inefficient due to the large scale of datasets. Various methods based on convex optimization have been proposed, such as the conjugated gradient method, Gauss–Newton method, and interior-point method, etc. [33]–[35]. Recently, the quadratic penalty (i.e., L2 regularization) is widely used, since it is simple and can be efficiently solved by a large range of standard minimization algorithms, such as Tikhonov method. However, the fast spatial changes in the solution are often smoothed, and the localized features can be lost during the reconstruction process [36], [37]. Unlike L2 regularization, L1 regularization can effectively suppress spurious background signals and enforce sparsity, which can preserve more details.

Manuscript received September 15, 2014; accepted February 14, 2015. Date of publication February 20, 2015; date of current version June 16, 2015. This work was supported by the National Basic Research Program of China (973 Program) under Grant 2011CB707700, the National Natural Science Foundation of China under Grants 81227901, 61231004, 81470083 and 30970777, the Key Research Program of the Chinese Academy of Sciences under Grant NO. KGZD-EW-T03, the Chinese Academy of Sciences Fellowship for Young Foreign Scientists under Grant No. 2010Y2GA03, 2013Y1GA0004, the Chinese Academy of Sciences Visiting Professorship for Senior International Scientists under Grant No. 2012T1G0036, 2013T1G0013. National Science and Technology Support Program 2012BAI23B01, and the Fundamental Research Funds for the Central Universities 2014YJS031 and 2014JBM026. *Asterisk indicates corresponding author.*

Y. An and G. Zhang are with the Beijing Jiaotong University.

*J. Liu is with the Department of Biomedical Engineering, School of Computer and Information Technology, Beijing Jiaotong University, Beijing 100044, China (e-mail: jieliu@bjtu.edu.cn).

J. Ye, Y. Du, and Y. Mao are with the Chinese Academy of Sciences.

*C. Chi and *J. Tian are with the Key Laboratory of Molecular Imaging of Chinese Academy of Sciences, Institute of Automation, Chinese Academy of Sciences, Beijing 100190, China (e-mail: chongwei.chi@ia.ac.cn; tian@ieee.org).

Color versions of one or more of the figures in this paper are available online at http://ieeexplore.ieee.org.

Digital Object Identifier 10.1109/TBME.2015.2404915

Consistent efforts are still being made to develop more advanced reconstruction methods for FMT. In this study, we proposed a novel region reconstruction method called the L1 regularization piecewise constant level set (L1-PCLS) approach, which are aimed at increasing the accuracy and efficiency of the reconstruction. In addition to describing the characteristics of the fluorescent regions, we consider *a priori* information encompasses the sparsity and contrast of the fluorescent sources. Here, we exploit the fact that while certain fluorescent probes target specific biological tissues such as tumors, the fluorescent intensities of target tissues and nominal background have obvious contrast [38]–[40]. Between different targets, we assume that the fluorescent intensities have a similarity to a certain degree, which is feasible when the targets are conducted with the same cells and the concentration of the probe is uniform. To accurately and effectively solve the L1-PCLS model, the alternating direction method and conjugate gradient (CG) [24] were employed. Some acceleration techniques designed for iteration of L1-PCLS were utilized to increase the efficiency of the algorithms.

The remainder of this paper is organized as follows. In Section II, we provide the forward diffusion approximation model and the L1-PCLS model of FMT is introduced briefly. In Section III, numerical heterogeneous phantom experiments are performed to validate the performance of the proposed method. Then, an *in vivo* bead-implanted mouse experiment is used to demonstrate the feasibility of L1-PCLS in *in vivo* application. The results are discussed and this paper is concluded in Section IV.

II. Methods

A. Photon Propagation Model

For steady-state FMT with point excitation source, the photon propagation model in highly scattering media such as biological tissues is based on the diffusion equation (DE) [41]. The following coupled DEs with a Robin-type boundary condition can be utilized to depict the forward problem [42], [43]

$$\begin{cases} \nabla \cdot (D_x(r)\nabla\Phi_x(r)) - \mu_{ax}(r)\Phi_x(r) = -\Theta\delta(r - r_l) \\ \nabla \cdot (D_m(r)\nabla\Phi_m(r)) - \mu_{am}(r)\Phi_m(r) \\ \quad = -\Phi_x(r)\eta\mu_{af}(r)(r \in \Omega) \\ 2D_{x,m}(r)\nabla\Phi_{x,m}(r) + v\Phi_{x,m}(r) = 0 \end{cases} \tag{1}$$

where r denotes the position of the point inside the image domain Ω. The subscripts x and m denote the excitation and emission light, respectively. $\Phi_{x,m}(r)$ is the photon flux density. $\mu_{ax,am}$ is the absorption coefficient, and $\mu_{sx,sm}$ is the scattering coefficient. $D_{x,m} = 1/3(\mu_{ax,am} + (1-g)\mu_{sx,sm})$ is the diffusion coefficient, and g is the anisotropy parameter. $\eta\mu_{af}(r)$ denotes the fluorescent field which is to be reconstructed, and v denotes the optical reflective index mismatch at the boundary. In this model, the excitation source is implemented as the isotropic point source, which is located one mean free path of photon transport beneath the surface [see Fig. 1(a)]. Θ denotes the amplitude of the excitation source.

By utilizing the finite element formulation to discretize the photon propagation model, we established the linear relationship between the measurements of the photon distribution on the surface and the unknown internal photon distribution by replacing the variables with the linear matrix equation

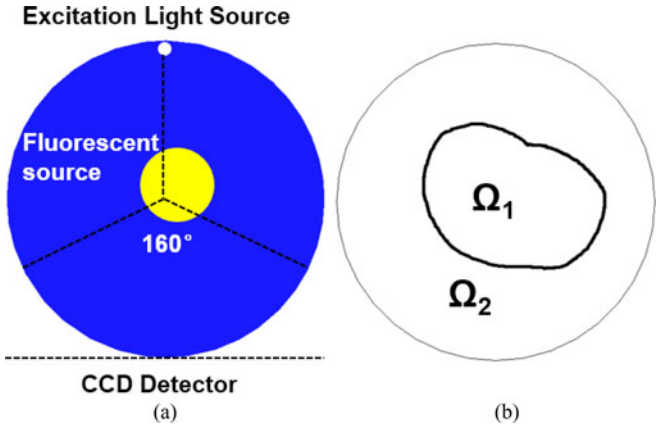

Fig. 1. (a) Setup of excitation light source and CCD detector for reconstruction. The FOV is 160° for CCD detection. (b) Definition of domains used for PCLS in cross-sectional view.

$$\Phi = AX \tag{2}$$

where Φ denotes the measurements of FMT, A denotes the system weight matrix and X denotes the intensity of the fluorescence distribution in biological tissues. Detailed descriptions can be found elsewhere [14], [15]. Therefore, solving the FMT inverse problem is aimed at recovering the fluorescent distribution X in the aforementioned linear matrix equation.

B. Region Reconstruction Method for FMT

The inverse problem of FMT is aimed at reconstructing the fluorescent targets according to (2), which can be directly solved by inverting the weight matrix A. However, this inversion is often ill-posed due to the fact that the dimension of Φ is usually much less than the dimension of X, which makes A not a square matrix, and the dimension of the null space of A is not zero. Hence, (2) needs to be regularized in order to achieve a robust solution. To guarantee the uniqueness and stability of FMT and to preserve the details of fluorescent regions, the L1-norm regularization is adopted in this paper. The optimization function with respect to (2) is formulated as follows:

$$\min_X E(X) = \arg\min_{X \geq 0} \frac{1}{2}||AX - \Phi||_2^2 + \lambda||X||_1 \tag{3}$$

where λ is the regularization parameter used to balance the data fitting and L1 penalty.

To reconstruct the fluorescent regions inside the biological tissues, the image is assumed to be formed by piecewise constant objects of interest on an unknown background. The feasibility analysis is performed beforehand. For a domain $\Omega_1 \in \Omega$, which represents the support of the objects of interest (fluorescent region), and $\Omega_2 = D\backslash\Omega_1$ represents the homogeneous background, as shown in Fig. 1(b), the corresponding PCLS function describing the characteristic of the shape for each set

is defined as

$$\phi(r) = \begin{cases} 1, & r \in \Omega_1 \\ -1, & r \in \Omega_2. \end{cases} \tag{4}$$

Then the fluorescence distribution X can be written as

$$X(\phi, C) = c_1 H(\phi) + c_2(1 - H(\phi)) = \Psi C \tag{5}$$

where $C = [c_1, c_2]^T$, $\Psi = [H(\phi), 1 - H(\phi)]$. In this formulation, the unknown values are assumed as the constant concentration values of the anomaly (object of interest) and background, c_1 and c_2, respectively [34], [35]. The characteristic function $H(\phi)$ is defined as a smooth approximation of the step function and the Dirac delta function

$$H(\phi) = \begin{cases} 1, & \phi > 1 \\ 0, & \phi < -1 \\ (1 + 4\arctan(\phi)/\pi)/2, & |\phi| <= 1. \end{cases} \tag{6}$$

To avoid the bound overflow in region reconstruction, an additional constraint function $K(\phi)$ is defined as

$$K(\phi) = \phi^2 - 1 = 0. \tag{7}$$

In summary, the optimization problem of the region reconstruction for FMT is

$$\min_X E(X) = \min_{\phi, c} E(X(\phi, C)), \quad \text{subject to } K(\phi) = 0. \tag{8}$$

eq.(8) for the FMT system is clearly convex. To solve (8), the augmented Lagrangian-based method is employed, which is a combination of the multiplier method and the penalization method

$$L(\phi, C, \eta, \mu) = E(\phi, C) + \int_\Omega \eta K(\phi) dr + \frac{1}{2}\mu \int_\Omega K^2(\phi) dr \tag{9}$$

where η is a parameter vector called the Lagrange multiplier, μ is a positive real number called a penalization parameter, and the last term of (9) is a penalization term. Note that when $K(\phi) = 0$, then the Lagrangian term vanishes, and $L = E$. Thus, the optimization point of (9) is equal to the solution of (8). At the optimization point of L, we must have

$$\frac{\partial L}{\partial \phi} = 0, \frac{\partial L}{\partial C} = 0, \frac{\partial L}{\partial \eta} = 0. \tag{10}$$

Since solving (10) for ϕ, C and η simultaneously is difficult and time-consuming, we follow the idea in the classic alternating direction method for solving these parameters. The flowchart of the proposed method is illustrated in Fig. 2.

First, consider the optimization of the level set function ϕ, which is realized via a gradient-based method [36], and an artificial time variable Δt is introduced

$$\tilde{\phi}^{k+1} = \tilde{\phi}^k - \Delta t \frac{\partial L}{\partial \tilde{\phi}^k}(\tilde{\phi}^k, C^k, \eta^k) \tag{11}$$

where $k = 0, 1, 2, \ldots, N$ is the iteration number, and N is the maximum iteration number. To make the iteration continuous, ϕ is replaced by a smoothed approximation $\tilde{\phi}$ with an amplitude

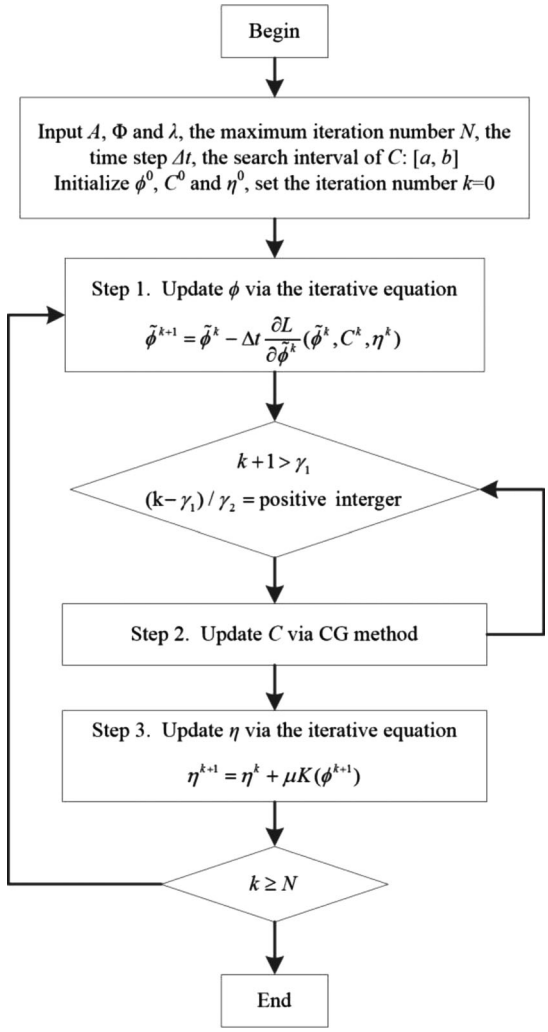

Fig. 2. Flow chart of the region reconstruction method.

parameter ε, which is a positive number much smaller than 1

$$\tilde{\phi} \approx \frac{\phi}{\sqrt{\phi^2 + \varepsilon}}. \tag{12}$$

Second, to consider the optimization of C, we need to calculate the equation

$$\begin{aligned} \frac{\partial L}{\partial C^k} &= \frac{\partial E}{\partial C^k} = \frac{\partial E}{\partial X^k}\frac{\partial X^k}{\partial C^k} \\ &= [A^T(A\Psi^k C^k - \Phi) + \lambda I]\Psi^k = 0. \end{aligned} \tag{13}$$

It is worth mention that $\Psi \neq 0$ in iteration of ϕ. Thus, the coefficient matrix of (12) will be zero, which leads to the equation

$$A^T A \Psi^k C^k = A^T \Phi - \lambda I. \tag{14}$$

We adopt the CG algorithm [24] to update C when solving (14). Due to the highly ill-posedness process in FMT, the updating procedure should not be implemented too early or too frequently during the iterations. Thus, a fixed number of iterations γ_1 and frequency γ_2 are used to constrain the iterations of C. Practically, the value of C is constrained in a predefined

search interval $[a, b]$ to further stabilize the iteration of C and restrain the produced value within a given range.

Last, an updating scheme for η is constructed which the form of the equation is same as the iteration equation of ϕ:

$$\eta^{k+1} = \eta^k + \mu K(\phi^{k+1}). \tag{15}$$

As the iterative intermediate result is close to the true optimization point, the iteration slows down. In Steps 1 and 3, the parameters ε and μ need to perform minor adjustment to accelerate the iteration. One other thing to note is that neither ε nor μ should be too large, which will make the iteration unstable.

III. Results

In this section, numerical heterogeneous phantom experiments and an *in vivo* mouse experiment were carried out to validate the performance of the proposed method. All computational processes were completed on a personal computer with 2.9-GHz Intel Core i7 CPU and 4-GB RAM.

To quantify the reconstruction results, the position error (PE), contrast-to-noise ratio (CNR) and dice coefficient (Dice) were utilized in this paper. PE was defined to analyze the location error between the barycenter of the reconstruction region and real fluorescent region.

$$\mathrm{PE} = ||P_r - P_0||_2 \tag{16}$$

where $P = [x, y, z]$ represents the coordinate vector of the points, and P_r, P_0 are the barycenter of the reconstruction region and real fluorescent region, respectively.

CNR was introduced to indicate whether the reconstructed region could be clearly distinguished from the background [44].

$$\mathrm{CNR} = \frac{\mu_{\mathrm{VOI}} - \mu_{\mathrm{VOB}}}{\sqrt{w_{\mathrm{VOI}}\sigma^2_{\mathrm{VOI}} + w_{\mathrm{VOB}}\sigma^2_{\mathrm{VOB}}}} \tag{17}$$

where w_{VOI}, w_{VOB} are the weight factors of the volume of interest (VOI) and volume of background (VOB) relative to the entire image volume, while μ_{VOI}, μ_{VOB} are the mean values of VOI and VOB, and σ_{VOI}, σ_{VOB} are the respective standard deviations. In this paper, the VOI was defined according to a threshold of 30% of the maximum fluorescent intensity.

Dice coefficient was performed to validate the similarity of the reconstruction region and the real fluorescent region.

$$\mathrm{Dice} = \frac{2|S_r \cap S_0|}{|S_r| + |S_0|} \tag{18}$$

where S_r and S_0 are the point sets of the reconstruction region and the real fluorescent region, respectively.

A. Results of the Heterogeneous Phantom Experiments

Heterogeneous phantom experiments were conducted to evaluate the performance of the L1-PCLS method. The heterogeneous cylindrical phantom is visualized in Fig. 3, where Fig. 3(a) shows the 3-D view of the phantom, and Fig. 3(b) shows the cross-sectional view of the phantom at the $z = 0$ slice. The diameter and height of the phantom were both 20 mm. Four kinds of tissues (heart, lungs, bone and muscle) were used to construct

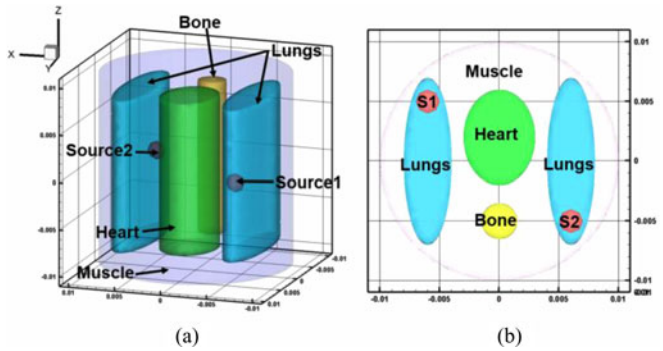

Fig. 3. Setups of the numerical phantom. (a) 3-D visualization of the phantom. (b) Cross-sectional view of the phantom at the $z = 0$ plane. S1 and S2 are two fluorescent sources set in the $z = 0$ plane. The diameter of the cylindrical phantom is 2 cm, and the diameter of the sources is 2 mm.

TABLE I
Optical Properties of the Numerical Phantom

Material	$\mu_{ax}\,(\mathrm{m}^{-1})$	$\mu_{sx}\,(\mathrm{m}^{-1})$	$\mu_{am}\,(\mathrm{m}^{-1})$	$\mu_{sm}\,(\mathrm{m}^{-1})$
Bone	2.4	1750	3.5	6.1
Lungs	13.3	1970	20.3	1950
Heart	8.3	1010	10.4	990
Muscle	5.2	1080	6.8	1030

the phantom, and the corresponding optical properties were assigned according to Table I [15]. The heterogeneous phantom was discretized to 4564 nodes and 24 333 elements for reconstruction. Two small spheres with a diameter of 2.0 mm each were embedded into the lungs to represent the real fluorescent regions. The excitation light sources were modeled as isotropic point sources located in the $z = 0$ slice with a light intensity of 0.02 W, and the measurements were taken in transillumination mode with a 160° field-of-view (FOV). Then, the photon propagation model and measurements were established using the finite element method. In the experiments, 5% Gaussian noise was added to the measurements to simulate the situation when practical fluorescence measurements were taken using a CCD camera. Fluorescent images in a 360° full view were collected at every 10° (i.e., 36 projections were adopted). To simulate the practical situation where the intensities of the fluorescent sources are similar to a certain degree, the intensity ratio for the two sources was set from 1:1 to 1:1.8 sequentially. To validate the reconstruction performance, two conventional methods (L1-IS and Tikhonov) were utilized to reconstruct the same datasets while maintaining the same termination condition.

The reconstruction results of the three methods with different fluorescent ratios are shown in Fig. 4, and the quantitative analysis of the performance for the three methods is listed in Table II. The columns of Fig. 4 denote the reconstruction results corresponding to different fluorescent ratios. The first, third and fifth rows in Fig. 4 illustrate the 3-D reconstruction results corresponding to Tikhonov, L1-IS and L1-PCLS, respectively, while the second, fourth and sixth rows illustrate the cross-sectional views corresponding to the three methods. The white circles in the cross-sectional views denote the real positions and regions

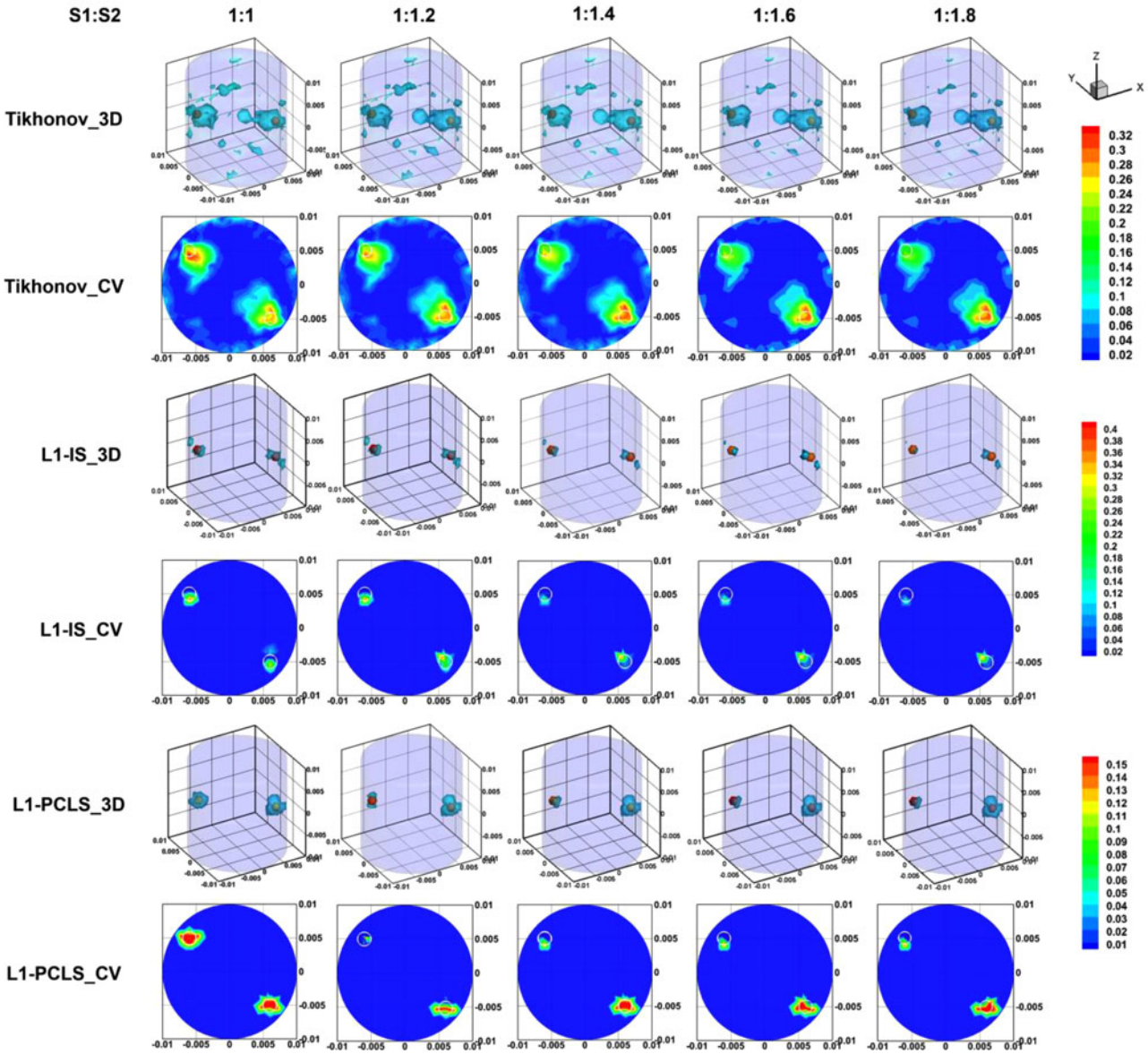

Fig. 4. Reconstructed results of heterogeneous numerical phantom experiments with different fluorescent ratios, using different methods. The columns denote the reconstructed results corresponding to different fluorescent ratios (S1:S2: 1:1, 1:1.2, 1:1.4, 1:1.6, 1:1.8). The first and second rows are the reconstruction results obtained using the Tikhonov method. The third and fourth rows correspond to the L1-IS method. The fifth and sixth rows correspond to the L1-PCLS method. −3-D denotes the 3-D views of the reconstruction results, and –CV denotes the cross-sectional views of the results. The red spheres in the 3-D views and the white circles in the cross-sectional views show the real positions of the fluorescent sources.

of the fluorescent sources. All the cross-sectional views in Fig. 4 are shown in the $z = 0$ slice.

To evaluate the performance of the reconstruction methods, the PE, CNR, dice coefficient and computation time were used to illustrate the robustness, accuracy and efficiency of the methods.

1) *Robustness:* When the intensity of S2 increased, the reconstruction results of the two targets became affected in both the Tikhonov and L1-IS according to the fact that the intensity of S1 was decreased in both methods. Particularly in L1-IS, the shape of S1 became more and more diminished. For the L1-PCLS, the intensities of the two targets were balanced due to the PCLS model, and the regions of the two targets robustly stayed the same when the intensity of S2 was bigger than S1. In fact, when the contrast of the two sources was too high (the fluorescent ratio is bigger than 1:2), all three methods could hardly obtain satisfactory reconstruction results. This is mainly because the reconstruction methods would automatically trade the weaker target as background.
2) *Accuracy:* L1-PCLS achieved better performance in PEs in both targets. When the fluorescent ratio increased, the PE for S1 increased, and the results were better than those obtained with the Tikhonov and L1-IS methods. Unlike the Tikhonov method, the results of the L1-regularization method acted out with a stronger convergence property and fewer reconstruction artifacts. However, for the region

TABLE II
QUANTITATIVE ANALYSIS OF THE THREE METHODS IN NUMERICAL PHANTOM EXPERIMENTS

Methods	Quantitative Index	Fluorescent Ratios (S1:S2)				
		1:1	1:1.2	1:1.4	1:1.6	1:1.8
Tikhonov	PE (mm)	S1:0.96	S1:0.96	S1:0.96	S1:0.96	S1:0.96
		S2:1.61	S2:1.61	S2:1.61	S2:0.58	S2:0.58
	CNR	11.2	11	11.2	11.5	12.2
	Dice	42%	41.1%	43.3%	40.8%	41.2%
	Time (s)	152.7	156.5	199.4	150.9	147.8
L1-IS	PE (mm)	S1:0.96	S1:1.34	S1:1.34	S1:0.96	S1:0.96
		S2:0.58	S2:0.93	S2:0.93	S2:0.93	S2:0.93
	CNR	47.5	40.1	51.4	63.0	73.4
	Dice	12.9%	9.5%	6.7%	6.7%	6.8%
	Time (s)	41.9	40.4	40.2	41.6	40.6
L1-PCLS	PE (mm)	S1:0.67	S1:0.42	S1:0.96	S1:0.96	S1:0.96
		S2:0.43	S2:0.43	S2:0.43	S2:0.43	S2:0.43
	CNR	45.3	45.5	47.9	47.9	47.9
	Dice	45.1%	22.6%	25.4%	25.4%	25.4%
	Time (s)	18.6	18.8	19.4	24.1	18.2

reconstruction, both the Tikhonov and L1-PCLS methods could achieve a high dice coefficient. Due to the high convergence property of L1-norm regularization, the CNRs of the L1-PCLS and L1-IS methods were much higher than for the Tikhonov. Owing to the balance effect of the PCLS model, the CNRs of the L1-PCLS method were not increasing infinitely.

3) *Efficiency:* For the same datasets, the Tikhonov method required nearly 150 s to implement the reconstruction, while the L1-IS considerably enhanced the efficiency up to nearly 40 s. Owing to the relatively simple model and accelerated techniques, the L1-PCLS took less computation time (nearly 20 s) to obtain satisfactory results compared to the other two methods. Consequently, the proposed method tended to be helpful and necessary.

B. Results of the In Vivo Mouse Experiments

To further study the potential of the proposed method in practical application of FMT, an *in vivo* experiment on an adult Kunming mouse (Laboratory Animal Center, Peking University, China) was performed with a dual-modality FMT and micro-CT imaging system previously developed by our group [45]–[47]. The schematic illustration of the system is shown in Fig. 5, which is mainly equipped with a cooled CCD camera, a continuous wave laser, a set of optical lenses, micro-CT equipment and a rotating stage. The fluorescence measurements were collected in transillumination mode.

The main process of *in vivo* experiments can be summarized as follows. At first, the mouse was implanted with a fluorescent bead in the hypogastria. The bead was filled with a cy5.5 solution with a concentration of 2000 nM, and this fluorescent solution had an extinction coefficient of 0.019 $\text{mm}^{-1}\mu\text{M}^{-1}$, with a quantum efficiency of 0.23 at the peak excitation wavelength of 671 nm, and the emission wavelength was 710 nm [48]. The performance of the proposed method can be accurately validated in this study, since the fluorescent bead was wrapped in a plastic material, which could be easily detected by the micro-CT system to locate the real fluorescent region. The detector FOV was 160° and eight projections were adopted. After obtaining the raw data including the fluorescence data and anatomical structural data, some essential preprocessing operations were carried out to prepare the data for FMT reconstruction. The original dataset acquired by micro-CT was converted into 3-D volume data via the Feldkamp–Davis–Kress algorithm [49], which is shown in Fig. 6. In order to build the heterogeneous mouse model, five main kinds of organs including muscle, lungs, heart, liver and kidneys were segmented through a combination method of interactive and region growing methods [47]. The optical properties for different organs were calculated according to [50], which is listed in Table III. Then, the fusion of the mesh and the

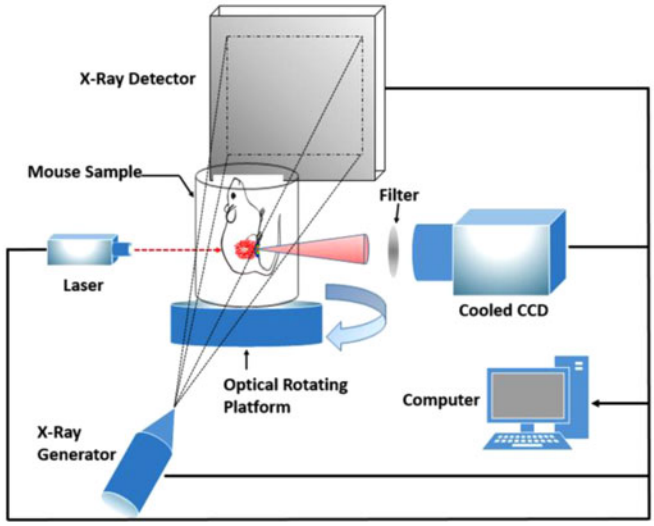

Fig. 5. Schematic diagram of the dual-modality FMT/micro-CT imaging system.

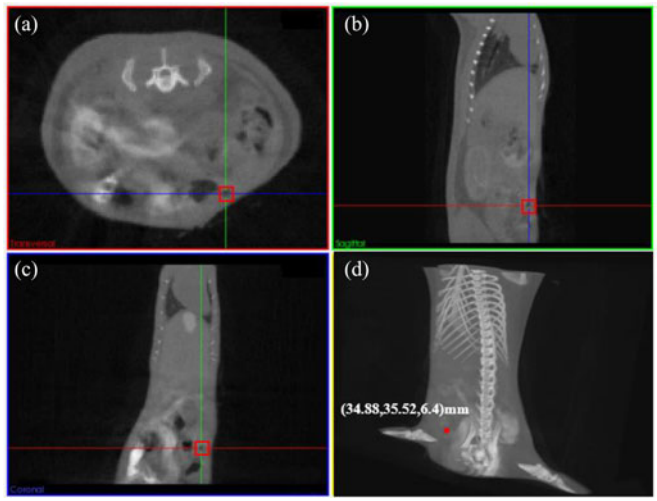

Fig. 6. Anatomical structure of the mouse. (a) Transverse view. (b) Coronal view. (c) Sagittal view. (d) 3-D visualization of the mouse. The red square marker in (a), (b) and (c), and the red dot marker in (d) illustrate the location of the fluorescent bead.

TABLE III
OPTICAL PROPERTIES OF THE *In Vivo* MOUSE EXPERIMENT

Material	$\mu_{ax}\,(\mathrm{m}^{-1})$	$\mu_{sx}\,(\mathrm{m}^{-1})$	$\mu_{am}\,(\mathrm{m}^{-1})$	$\mu_{sm}\,(\mathrm{m}^{-1})$
Liver	343.67	677	228.31	648
Lungs	191.82	2172	126.55	2124
Heart	57.45	962	38.29	905
Kidneys	64.45	2248	43.03	2109
Muscle	84.95	427.3	56.3	379.2

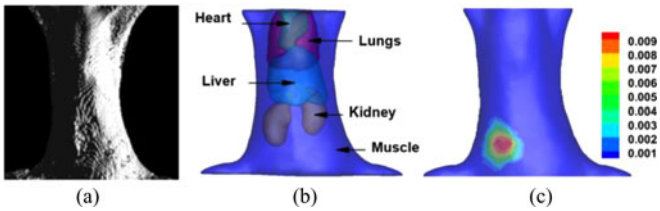

Fig. 7. Heterogeneous mouse model for the *in vivo* experiment. (a) Surface of the mouse body. (b) Heterogeneous mouse torso used for imaging reconstructions, including heart, lungs, liver, muscle, and kidneys. (c) Surface view of the mouse torso with the frontal view measurements mapped on it.

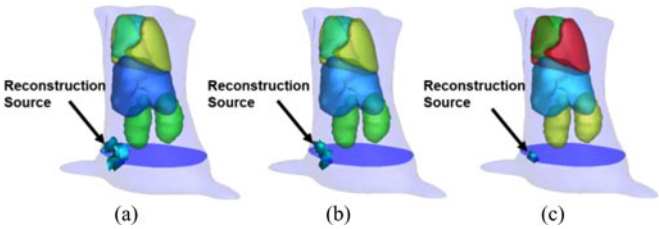

Fig. 8. 3-D views of the reconstruction results using Tikhonov, L1-IS and L1-PCLS methods. The blue plane in the figure is the $z = 6.4$ mm slice. (a)–(c) Reconstruction results by Tikhonov, L1-IS and L1-PCLS, respectively.

fluorescence data was carried out via a 3-D surface flux reconstruction algorithm [51]. The heterogeneous mouse model and the fusion are shown in Fig. 7. Finally, the heterogeneous mouse model was discretized into 5639 nodes and 33 627 elements for the reconstruction of FMT.

After finishing the above procedures, the reconstruction of FMT was performed by using three different reconstruction methods (Tikhonov, IS and L1-PCLS). The 3-D reconstruction results of the three methods are shown in Fig. 8. Fig. 8(a)–(c) are the reconstruction results by Tikhonov, L1-IS and L1-PCLS, respectively. The cross-sectional views of the results are given in Fig. 9, where Fig. 9(c), (d) and (g) are the cross-sectional views of Tikhonov, L1-IS and L1-PCLS, respectively. Fig. 9(a) shows the 3-D rendering of the experimental mouse and the location of the fluorescent bead, while Fig. 9(b), (d) and (f) are the cross-sectional views of the source location plane ($z = 6.4$ mm). The red squares denote the real position of the fluorescent bead. Quantitative analysis for the performance of the three methods is shown in Table IV, which is also conducted by PE, CNR, dice and computation time.

Similar to the heterogeneous phantom experiments, better reconstruction results were achieved by the proposed L1-PCLS

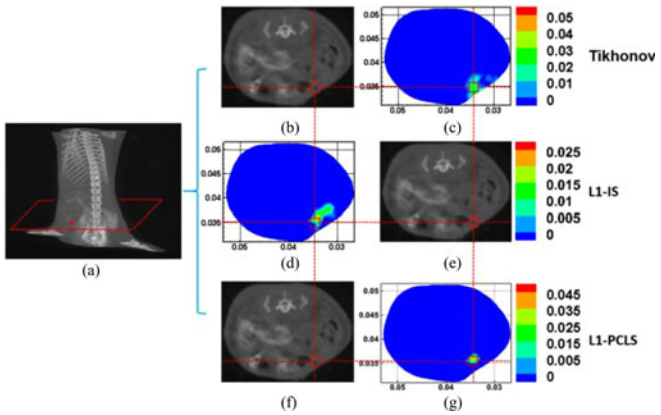

Fig. 9. Cross-sectional views of the *in vivo* region reconstruction results via the Tikhonov, L1-IS and L1-PCLS methods. The cross-sectional views of the reconstruction results are compared with the corresponding micro-CT slices. The red square markers denote the real position of the fluorescent bead. (a) 3-D rendering of the mouse, where the red plane is $z = 6.4$ mm, and the red dot marks the real position of the fluorescent bead. (c), (d) and (g) Lateral cross-sectional views of the reconstruction results obtained with Tikhonov, L1-IS and L1-PCLS, respectively. (b), (e) and (f) $z = 6.4$ mm micro-CT slices corresponding to (c), (d) and (g).

TABLE IV
QUANTITATIVE ANALYSIS OF THE THREE METHODS IN *In Vivo* EXPERIMENTS

Methods	PE (mm)	CNR	Dice	Time (s)
CG	1.525	3.56	19.8%	72.2
IS	0.669	5.02	33.4%	21.6
L1-PCLS	0.320	8.34	89.1%	10.1

method. Owing to the number of projections for the *in vivo* study is much less than the phantom study, there were more reconstruction artifacts via Tikhonov and L1-IS methods, as shown in Figs. 8 and 9. Even in this adverse situation, the proposed method could still obtain satisfactory results. Quantitative analysis of the performance has further demonstrated the superiority of L1-PCLS. This means that the proposed method could achieve reliable fluorescent targets in biological application.

IV. DISCUSSION AND CONCLUSION

In this paper, we propose a novel region reconstruction method called L1-PCLS to reconstruct the internal fluorescent regions for FMT. It is well known that the ill-posedness of the FMT inverse problem causes relatively large errors in reconstruction. There are various kinds of methods based on convex optimization and compress sensing to reconstruct the fluorescent distributions inside biological tissues [14]–[16]. In addition, compression methods have been proposed for reducing the computational complexity of FMT [52], [53]. To solve the ill-posedness problem of FMT, the sparsity and contrast of the fluorescent region is used as *a priori* knowledge, and accordingly L1-norm regularization and PCLS is performed in the proposed method. Because the L1-PCLS function for FMT is clearly convex, we adopt the augmented Lagrangian-based method, which is a conventional tool to solve the problem of convex

optimization. As the FMT inverse problem is severely ill-posed and the parameters of Lagrangian objective function can hardly be solved simultaneously, the convergence speed of L1-PCLS will deteriorate. Thus, the alternating direction method and CG method are introduced to accelerate the iteration. With these approaches, the proposed method can reconstruct the characteristics of the fluorescent regions accurately and effectively. Owing to the sparsity constraint of L1-regularization and balance effect of PCLS, the reconstruction of L1-PCLS is neither oversmoothed nor overshrunk. Thus, L1-PCLS is a novel reconstruction strategy for FMT, and it can reconstruct satisfactory fluorescent targets inside biological tissues.

To validate the performance of L1-PCLS, we performed numerical heterogeneous phantom experiments and *in vivo* mouse experiments. For comparison, the L1-IS and Tikhonov methods were adopted. The experimental results indicated that L1-PCLS was capable of obtaining accurate features of the fluorescent regions. In numerical phantom experiments with the dual fluorescent source case and different fluorescent ratios, L1-PCLS maintained reliable reconstruction results, and the performance of the proposed method was illustrated via PE, CNR, and Dice coefficient of the reconstruction results. The reconstruction results of the *in vivo* mouse experiments validated the feasibility of L1-PCLS in an *in vivo* application, and the features of the reconstruction regions obtained by L1-PCLS were better than the two conventional methods, which demonstrated the superiority of the proposed method in *in vivo* application. Besides, the computation time of L1-PCLS was substantially satisfactory in both numerical phantom experiments and *in vivo* experiments, which illustrated the efficiency of the proposed method.

It should be noted that incorrect parameters used in the algorithms might reduce the performance of the proposed method. The adaptive parameter achievement algorithms should be studied further. Besides, other performances of the proposed method, such as spatial resolution and depth sensitivity, should be systematically tested.

REFERENCES

[1] H. Fan-Minogue *et al.*, "Noninvasive molecular imaging of c-Myc activation in living mice," *Proc. Nat. Acad. Sci. USA*, vol. 107, pp. 15892–15897, 2010.

[2] M. A. Whitney *et al.*, "Fluorescent peptides highlight peripheral nerves during surgery in mice," *Nat. Biotechnol.*, vol. 29, pp. 352–356, 2011.

[3] G. M. van Dam *et al.*, "Intraoperative tumor-specific fluorescence imaging in ovarian cancer by folate receptor-alpha targeting: First in-human results," *Nat. Med.*, vol. 17, pp. 1315–1319, 2011.

[4] C. Chi *et al.*, "Intraoperative imaging-guided cancer surgery: From current fluorescence molecular imaging methods to future multi-modality imaging technology," *Theranostics*, vol. 4, pp. 1072–1084, 2014.

[5] C. W. Chi *et al.*, "Use of indocyanine green for detecting the sentinel lymph node in breast cancer patients: From preclinical evaluation to clinical validation," *Plos One*, vol. 8, pp. 1–12, 2013.

[6] V. Ntziachristos, "Going deeper than microscopy: The optical imaging frontier in biology," *Nat. Methods*, vol. 7, pp. 603–614, 2010.

[7] F. G. Blankenberg and H. W. Strauss, "Recent advances in the molecular imaging of programmed cell death: Part II—Non-probe-based MRI, ultrasound, and optical clinical imaging techniques," *J. Nucl. Med.*, vol. 54, pp. 1–4, 2013.

[8] S. Keereweer *et al.*, "Optical image-guided surgery—Where do we stand?," *Mol. Imag. Biol.*, vol. 13, pp. 199–207, 2011.

[9] T. F. Massoud and S. S. Gambhir, "Molecular imaging in living subjects: Seeing fundamental biological processes in a new light," *Genes Dev.*, vol. 17, pp. 545–580, 2003.

[10] A. Ale *et al.*, "FMT-XCT: In vivo animal studies with hybrid fluorescence molecular tomography-X-ray computed tomography," *Nat. Methods*, vol. 9, pp. 615–620, 2012.

[11] F. Leblond *et al.*, "Toward whole-body optical imaging of rats using single-photon counting fluorescence tomography," *Opt. Lett.*, vol. 36, pp. 3723–3725, 2011.

[12] J. K. Willmann *et al.*, "Molecular imaging in drug development," *Nat. Rev. Drug Discov.*, vol. 7, pp. 591–607, 2008.

[13] X. Song *et al.*, "Reconstruction for free-space fluorescence tomography using a novel hybrid adaptive finite element algorithm," *Opt. Exp.*, vol. 15, pp. 18300–18317, 2007.

[14] J. Shi *et al.*, "Efficient L1 regularization-based reconstruction for fluorescent molecular tomography using restarted nonlinear conjugate gradient," *Opt. Lett.*, vol. 38, pp. 3696–3699, 2013.

[15] D. Han *et al.*, "A fast reconstruction algorithm for fluorescence molecular tomography with sparsity regularization," *Opt. Exp.*, vol. 18, pp. 8630–8646, 2010.

[16] J. Ye *et al.*, "Fast and robust reconstruction for fluorescence molecular tomography via a sparsity adaptive subspace pursuit method," *Biomed. Opt. Exp.*, vol. 5, pp. 387–406, 2014.

[17] C. Li *et al.*, "A three-dimensional multispectral fluorescence optical tomography imaging system for small animals based on a conical mirror design," *Opt. Exp.*, vol. 17, pp. 7571–7585, 2009.

[18] A. J. Chaudhari *et al.*, "Excitation spectroscopy in multispectral optical fluorescence tomography: Methodology, feasibility and computer simulation studies," *Phys. Med. Biol.*, vol. 54, pp. 4687–4704, 2009.

[19] G. Zacharakis *et al.*, "Volumetric tomography of fluorescent proteins through small animals *in vivo*," *Proc. Nat. Acad. Sci. USA*, vol. 102, pp. 18252–18257, 2005.

[20] H. Gao and H. Zhao, "Multilevel bioluminescence tomography based on radiative transfer equation Part 1: l1 regularization," *Opt. Exp.*, vol. 18, pp. 1854–1871, 2010.

[21] V. C. Kavuri *et al.*, "Sparsity enhanced spatial resolution and depth localization in diffuse optical tomography," *Biomed. Opt. Exp.*, vol. 3, pp. 943–957, 2012.

[22] P. Mohajerani *et al.*, "Optimal sparse solution for fluorescent diffuse optical tomography: Theory and phantom experimental results," *Appl. Opt.*, vol. 46, pp. 1679–1685, 2007.

[23] S. Osher and J. A. Sethian, "Fronts propagating with curvature-dependent speed: Algorithms based on Hamilton-Jacobi formulations," *J. Comput. Phys.*, vol. 79, pp. 12–49, 1988.

[24] C. Samson *et al.*, "A level set model for image classification," *Int. J. Comput. Vision*, vol. 40, pp. 187–197, 2000.

[25] T. F. Chan and L. A. Vese, "Active contours without edges," *IEEE Trans. Image Process.*, vol. 10, no. 2, pp. 266–277, Feb. 2001.

[26] M. K. B. H. Miled and E. L. Miller, "A projection-based level-set approach to enhance conductivity anomaly reconstruction in electrical resistance tomography," *Inverse Problems*, vol. 23, pp. 2375–2400, 2007.

[27] V. Kolehmainen *et al.*, "Limited data X-ray tomography using nonlinear evolution equations," *SIAM J. Sci. Comput.*, vol. 30, pp. 1413–1429, 2008.

[28] D. F. Yu and J. A. Fessler, "Edge-preserving tomographic reconstruction with nonlocal regularization," *IEEE Trans. Med. Imag.*, vol. 21, no. 2, pp. 159–173, Feb. 2002.

[29] F. Larusson *et al.*, "Parametric level set reconstruction methods for hyperspectral diffuse optical tomography," *Biomed. Opt. Exp.*, vol. 3, pp. 1006–1024, 2012.

[30] K. Liu *et al.*, "Spectrally resolved three-dimensional bioluminescence tomography with a level-set strategy," *J. Opt. Soc. Am. A Opt. Image Sci. Vis.*, vol. 27, pp. 1413–1423, 2010.

[31] J. Lie *et al.*, "A binary level set model and some applications to Mumford-Shah image segmentation," *IEEE Trans. Image Process*, vol. 15, no. 5, pp. 1171–1181, May 2006.

[32] O. Semerci and E. L. Miller, "A parametric level-set approach to simultaneous object identification and background reconstruction for dual-energy computed tomography," *IEEE Trans. Image Process*, vol. 21, no. 5, pp. 2719–2734, May 2012.

[33] M. Schweiger *et al.*, "Gauss-Newton method for image reconstruction in diffuse optical tomography," *Phys. Med. Biol.*, vol. 50, pp. 2365–2386, 2005.

[34] W. Zhu *et al.*, "Iterative total least-squares image reconstruction algorithm for optical tomography by the conjugate gradient method," *J. Opt. Soc. Am. A Opt. Image Sci. Vis.*, vol. 14, pp. 799–807, 1997.

[35] D. M. Aleman *et al.*, "Interior point algorithms: Guaranteed optimality for fluence map optimization in IMRT," *Phys. Med. Biol.*, vol. 55, pp. 5467–5482, 2010.
[36] J. Dutta *et al.*, "Joint L1 and total variation regularization for fluorescence molecular tomography," *Phys. Med. Biol.*, vol. 57, pp. 1459–1476, 2012.
[37] D. Han *et al.*, "Efficient reconstruction method for L1 regularization in fluorescence molecular tomography," *Appl. Opt.*, vol. 49, pp. 6930–6937, 2010.
[38] X. B. Ma *et al.*, "SM5-1-conjugated PLA nanoparticles loaded with 5-fluorouracil for targeted hepatocellular carcinoma imaging and therapy," *Biomaterials*, vol. 35, pp. 2878–2889, 2014.
[39] A. Cerussi *et al.*, "Predicting response to breast cancer neoadjuvant chemotherapy using diffuse optical spectroscopy," *Proc. Nat. Academy Sci. USA*, vol. 104, pp. 4014–4019, 2007.
[40] M. J. Uddin *et al.*, "Selective visualization of cyclooxygenase-2 in inflammation and cancer by targeted fluorescent imaging agents," *Cancer Res.*, vol. 70, pp. 3618–3627, 2010.
[41] Y. Tan and H. Jiang, "DOT guided fluorescence molecular tomography of arbitrarily shaped objects," *Med. Phys.*, vol. 35, pp. 5703–5707, 2008.
[42] A. Joshi *et al.*, "Adaptive finite element based tomography for fluorescence optical imaging in tissue," *Opt. Exp.*, vol. 12, pp. 5402–5417, 2004.
[43] J. H. Lee *et al.*, "Fully adaptive finite element based tomography using tetrahedral dual-meshing for fluorescence enhanced optical imaging in tissue," *Opt. Exp.*, vol. 15, pp. 6955–6975, 2007.
[44] C. Chen *et al.*, "Diffuse optical tomography enhanced by clustered sparsity for functional brain imaging," *IEEE Trans. Med. Imag.*, vol. 33, no. 12, pp. 2323–2331, Dec. 2014.
[45] C. Qin *et al.*, "New optical molecular imaging systems," *Curr. Pharm. Biotechnol.*, vol. 11, pp. 620–627, 2010.
[46] S. Zhu *et al.*, "Cone beam micro-CT system for small animal imaging and performance evaluation," *Int. J. Biomed. Imag.*, vol. 2009, art. no. 960573, pp. 1–9, 2009.
[47] W. Ping *et al.*, "Bioluminescence tomography by an iterative reweighted (l)2 norm optimization," *IEEE Trans. Biomed. Eng.*, vol. 61, no. 1, pp. 189–196, Jan. 2014.
[48] F. Gao *et al.*, "A linear, featured-data scheme for image reconstruction in time-domain fluorescence molecular tomography," *Opt. Exp.*, vol. 14, pp. 7109–7124, 2006.
[49] G. R. Yan *et al.*, "Fast cone-beam CT image reconstruction using GPU hardware," *J. X-Ray Sci. Technol.*, vol. 16, pp. 225–234, 2008.
[50] G. Alexandrakis *et al.*, "Tomographic bioluminescence imaging by use of a combined optical-PET (OPET) system: A computer simulation feasibility study," *Phys. Med. Biol.*, vol. 50, pp. 4225–4241, 2005.
[51] X. Chen *et al.*, "3D reconstruction of light flux distribution on arbitrary surfaces from 2D multi-photographic images," *Opt. Exp.*, vol. 18, pp. 19876–19893, 2010.
[52] N. Ducros *et al.*, "Multiple-view fluorescence optical tomography reconstruction using compression of experimental data," *Opt. Lett.*, vol. 36, pp. 1377–1379, 2011.
[53] P. Mohajerani and V. Ntziachristos, "Compression of born ratio for fluorescence molecular tomography/x-ray computed tomography hybrid imaging: Methodology and *in vivo* validation," *Opt. Lett.*, vol. 38, pp. 2324–2326, 2013.

Authors' photographs and biographies not available at the time of publication.